J. Fluid Mech. (1975), *vol.* 68, *part* 1, *pp.* 49–70
Printed in Great Britain

Wind-induced drift currents

By JIN WU

College of Marine Studies, University of Delaware, Newark
and Hydronautics, Inc., Laurel, Maryland

(Received 6 March 1974)

Systematic measurements of drift currents below and of airflows above an air–water interface have been made under various wind conditions. The current near but not immediately below the water surface is found to follow a Kármán–Prandtl (logarithmic) velocity distribution. The current immediately below the water surface varies linearly with depth. The transitions of the current boundary layer to various regimes appear to lag behind, or to occur at a higher wind velocity than, those of the airflow. The fraction of the wind stress supported by the wave drag seems to vary with the wind and wave conditions: a large fraction is obtained at low wind velocities with shorter waves and a small fraction is obtained at high wind velocities with longer waves. At the air–water interface, the wind-induced current is found to be proportional to the friction velocity of the wind. The Stokes mass transport, related to wave characteristics, is only a small component of the surface drift in laboratory tanks. However, in terms of the fraction of the wind velocity, the mass transport increases, while the wind drift decreases, as the fetch increases. The ratio between the total surface drift and the wind velocity decreases gradually as the fetch increases and approaches a constant value of about 3·5 % at very long fetches.

1. Introduction

Recent intensive studies and measurements of wind–wave interactions seem to have concentrated principally on phenomena at and above the air–water interface. The wind-induced drift current in the upper layer just below the interface, an important part of the mutually interacting air–sea system, has been investigated only fragmentarily (Keulegan 1951; Baines & Knapp 1965; Bye 1965; Plate 1970; Shemdin 1972). The studies of Keulegan and Plate concentrated on the surface drift, Baines & Knapp measured the drift profiles for low wind velocities in a shallow channel and Bye and Shemdin observed the logarithmic current distribution within a limited range of wind velocities. The drift current not only governs momentum, mass and heat transfer processes across the interface, but also dissipates the energy introduced by the wind into the system. These dynamical processes are directly related to global weather and ocean circulation. Furthermore, the drift current, having a steep gradient near the water surface, influences to a large extent the diffusion, dispersion and drift of foreign masses, such as pollutants, discharged into natural bodies of water (Wu 1969*a*).

Systematic measurements of drift currents using various techniques (surface floats, submerged floats and a traversing probe) and under various wind conditions are reported here. The profiles of the drift currents and the regimes of the current boundary layers are discussed and compared with those of the wind. The friction velocities of the wind and of the current are determined from the velocity profiles, and the difference, the wave drag, is found to vary with wave conditions. On the basis of the present results for drift currents and available field data on dominant waves, the wind-induced surface drifts at various fetches are estimated. It is hoped that the results will be helpful on the one hand for understanding the dynamics of wind-driven currents, and on the other hand for meeting practical needs of predicting drift currents near the water surface.

2. Experiment

Wind–wave tank

The wind–wave tank, shown in figure 1 (*a*), is 1·5 m wide, 1·55 m deep and about 22 m long. Mounted at the upwind end of the tank is an axial-flow fan driven by a variable-speed motor; a permeable wave absorber is installed at the downwind end. The air is sucked, passing through guiding vanes, into the tank, which is covered for the first 16 m. The maximum wind velocity obtainable within a 31 cm high wind tunnel above 124 cm deep water is 15 m/s. The test section is located at the 11 m station, being equidistant from the ends of the tank, where the mean water surface is least affected by the wind-induced set-up of the water surface.

Wind and wave measurements

The wind velocity profile in the tunnel was determined by vertically traversing a Pitot–static tube supported on a precise travelling mechanism. During the experiment, the tube was driven downwards from a given elevation at a small and constant speed of 2·5 cm/min to measure the wind boundary layer near the water surface. The velocity head, sensed by a differential pressure transducer, was continuously recorded on an x, y plotter.

A conductivity probe was used for wave measurements. The probe has a partially submerged platinum wire 0·25 mm in diameter as one electrode with a fully submerged aluminium plate acting as the other. The output of the probe, the electric current flowing between two electrodes, is proportional to the submergence of the wire. The probe output, the temporal variation of the water level at a fixed location, was continuously recorded on a visicorder.

Current measurements

Surface and near-surface drift current. The drift current immediately below the water surface was measured by timing floats of various sizes passing two stations 1·5 m upwind and downwind from the test section respectively. Spherical particles of three different sizes and a thin circular disk were used as surface floats. The specific gravity of the floats is 0·95. The velocity of a float was interpreted as the drift current at the depth of the centroid of the longitudinally projected

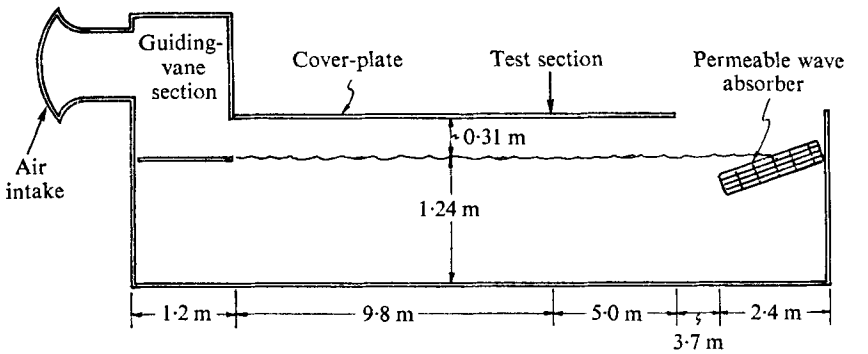

(*a*)

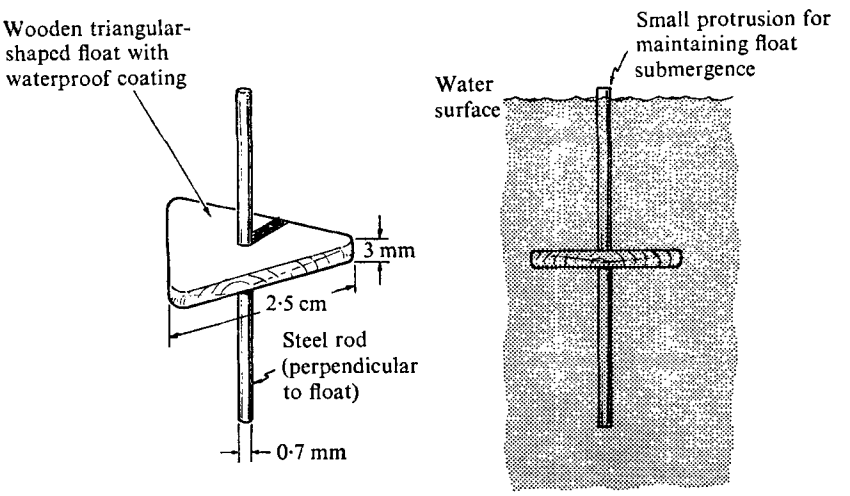

(*b*)

FIGURE 1. (*a*) General arrangement and (*b*) submerged floats.

area of the submerged portion of that float. The surface drift current was determined by extrapolating the current distribution curve to the water surface. This technique (Wu 1968) therefore provides measurements of the surface drift as well as of near-surface profiles. It is also convenient at high wind velocities, where breaking waves tend to sink small thin floats.

Subsurface drift current. A Pitot–static tube was supported at various depths below the mean water surface for the subsurface current measurements. At each depth, the velocity head, sensed by a differential pressure transducer, was continuously recorded on a tape recorder for a period of 2 min. The tape was later played back on an analog computer at a sampling interval of 0·01 s to determine the average drift current.

As the Pitot–static tube approached the interface, the surface undulation made measurements with a fixed probe impossible. Submerged floats, as shown in

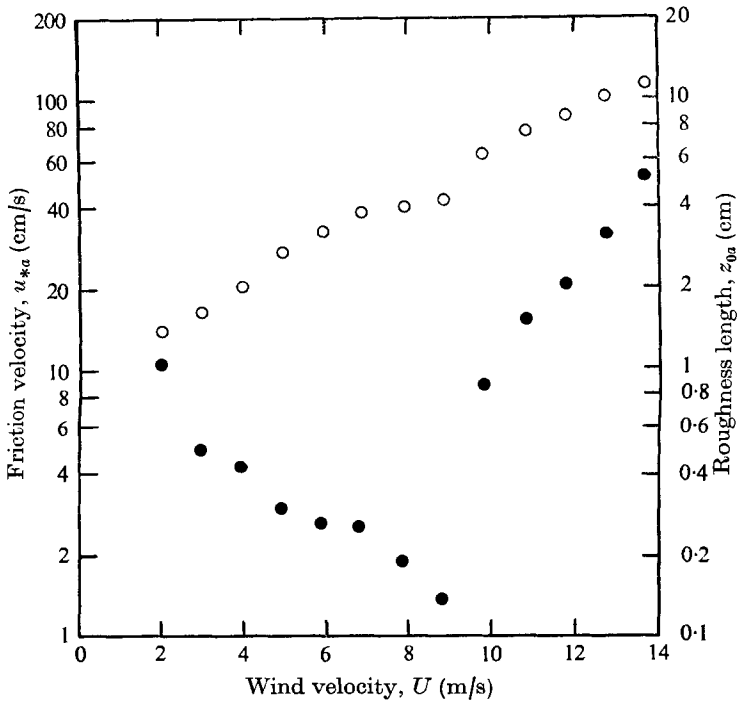

FIGURE 2. Friction velocity of wind (open circles) and roughness length of wind boundary layer (solid circles).

figure 1 (*b*), were designed and used for *near-surface* current measurements. These floats consist of a triangular plywood disk and a normal metal stem. Stems of various lengths were used to make the floats neutrally buoyant with the disks submerged at desired depths. In order to avoid wind effects on the floats, the top of the stem only just protruded above the water surface, but this small protrusion was essential for stabilizing the floats at the designated depths. The floats were observed to maintain their constant submergence in the wind–wave tank. Tests were conducted by changing the protrusion of the stem; the floats were observed to return quickly to their designated depths with very little bobbing. The floats were timed between two stations along the tank and the speed of each float was interpreted as the longitudinally averaged current at the disk submergence.

3. Wind and wave conditions

Wind

The wind velocity profile in the tunnel was found, as reported earlier (Wu 1968), to follow the logarithmic law (Schlichting 1968, p. 582) near but not too close to the water surface. The friction velocity u_{*a} of the wind and the roughness length z_{0a} of the wind boundary layer, determined from the wind profile, are plotted in figure 2, where U is the free-stream wind velocity. It should be

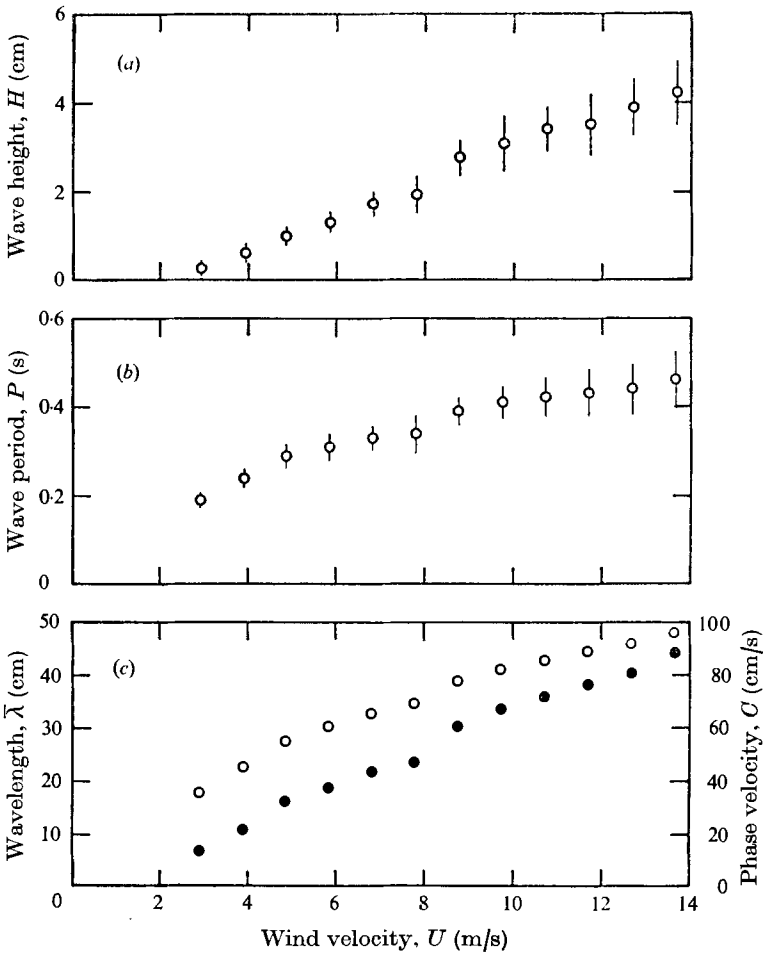

FIGURE 3. Wave heights, wave periods, wavelengths and phase velocities for various wind velocities. ●, $\bar{\lambda}$; ○, C.

emphasized here that, because of the differences between scales under oceanic and laboratory conditions and because of the differences in the wind structure in various wind–wave tanks, the wind data shown in figure 2 have no general application.

Waves

Observation of wave growth in the present tank showed that infinitesimal capillary waves were first generated at a very low wind velocity $U < 1{\cdot}9$ m/s. Rhombic gravity wave cells were formed as soon as the wind boundary layer became turbulent. As the wind velocity increased beyond 3·5 m/s, parasitic capillaries were first produced; this is the regime of wind–wave interaction governed by surface tension (Wu 1968). Wave breaking was observed at high wind velocities $U > 9{\cdot}5$ m/s, where gravity replaced surface tension as the governing parameter of the wind–wave interaction.

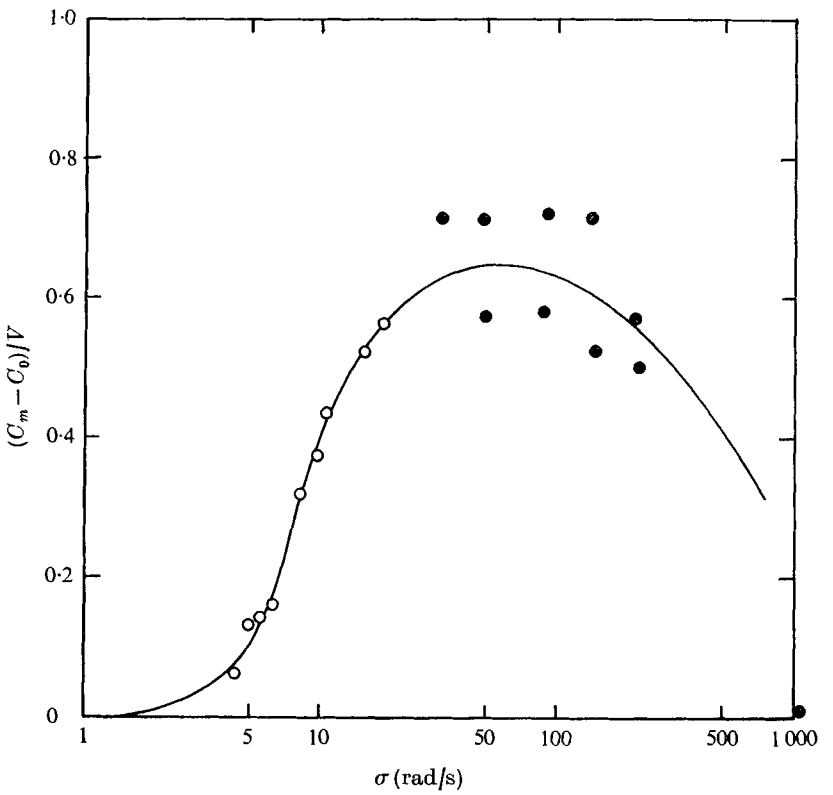

FIGURE 4. Influence of wind drift on wave propagation. ○, Shemdin (1972); ●, Wright & Keller (1971).

From the records, the periods and heights of more than 100 basic waves were obtained for each wind velocity. The wind waves generated in the tank were narrow banded. The standard deviations of the data for both wave periods and wave heights were found to be generally less than 20 % of the average values. The average wave (trough to peak) heights H and wave periods P obtained at various wind velocities are plotted, along with the standard deviations, shown as short vertical lines, in figures 3(*a*) and (*b*).

It is known (Cox 1958; Wright & Keller 1971; Shemdin 1972) that the phase velocity of a wind-generated wave is greater than that indicated by the dispersion relationship

$$C_0^2 = g\lambda/2\pi + 2\pi T/\rho\lambda, \tag{1}$$

where C_0 is the phase velocity, g is the gravitational acceleration, λ is the wavelength, T is the surface tension and ρ is the density of water. The correction factor, the difference between measured and calculated phase velocities, was related to the free-stream wind velocity by Shemdin (1972). However the surface drift current is the logical reference quantity because the ratio between the surface drift current and the wind velocity has been found (Wu 1968; Wright & Keller 1971) to vary from tank to tank. The correction factor, reparameterized in terms of the surface drift current, is plotted in figure 4. In this figure, C_m is the measured

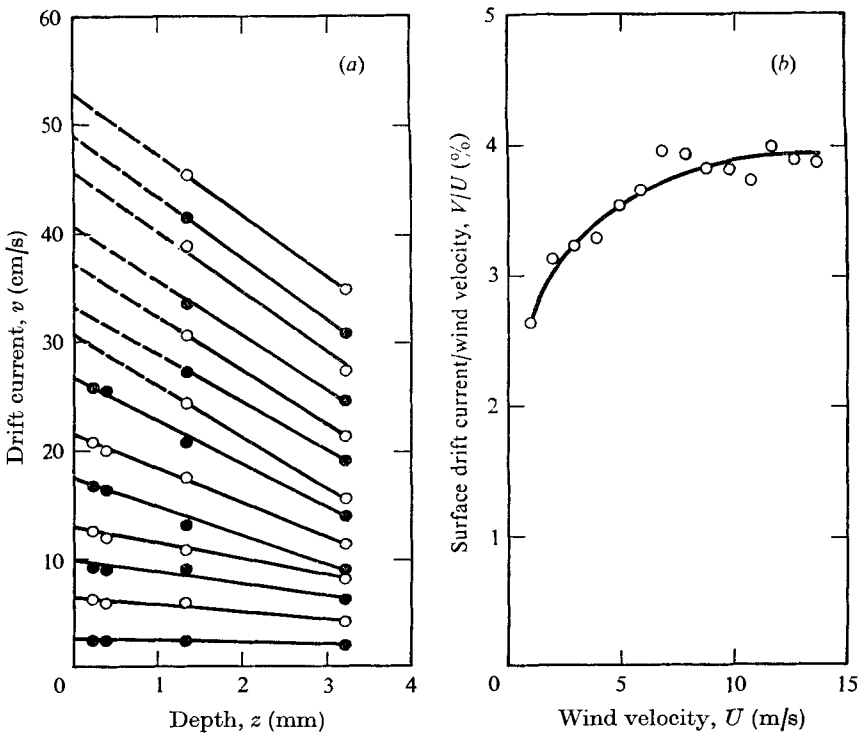

FIGURE 5. Surface drift currents measured for various wind velocities. The current distributions shown in (*a*) from bottom to top were obtained in the order of increasing wind velocities. The surface current shown in (*b*) was obtained by extending the distribution curve to the water surface.

phase velocity of the waves, V is the surface drift current and σ is the radian wave frequency ($\sigma = 2\pi/P$). A curve was fitted to the data to relate the correction factor empirically to the radian wave frequency.

More studies are required to understand the effects of wind drift on wave propagation, however the expression showing that the wind drift has less effect on longer waves is certainly sound. On the basis of the correction line shown in figure 4 and the surface drift current to be shown later, the phase velocity C and the wavelength $\bar{\lambda}$ of the average (dominant) wave were calculated and are plotted in figure 3(*c*).

4. Surface drift currents

Determination of surface drift current

The vertical distributions of the drift current at different wind velocities are shown in figure 5(*a*), where each data point represents the average of more than 10 measurements. The standard deviation of the measured float speed was found generally to be within 10% of the average value. The drift current v appears to vary almost linearly with the depth z below the water surface. The exact shape of the distribution curve is hard to determine, especially at high wind

velocities. However, our main interest for this series of measurements is to determine the surface drift current by extrapolating the distribution curve to the water surface. As illustrated by the data shown in figure 5(*a*), a slight deviation of the current from a linear distribution within this shallow region near the water surface should not introduce any appreciable error in the surface drift current.

The surface drift current obtained, as shown in figure 5(*a*), from the intersection of the fitted straight line with the water surface is plotted versus the wind velocity in figure 5(*b*). A smooth curve has been drawn to indicate the variation of the surface drift current with wind velocity. As reported earlier (Keulegan 1951; Wu 1968), the surface drift current approaches an equilibrium fraction of the wind velocity as the wind blows harder and waves start to break.

Stokes surface transport

A slow but continuous forward motion of the particles in a water wave was theoretically predicted by Stokes (1847). The rate v_w of this flow at a mean water depth D was expressed as

$$v_w = (\pi H/\lambda)^2 C_0 \exp(-4\pi D/\lambda). \tag{2}$$

The Stokes transport V_w at the water surface can therefore be estimated from

$$V_w = C_0(\pi H/\lambda)^2. \tag{3}$$

Experimental verifications of the above expressions have been provided by Russell & Osorio (1957) and Chang (1969).

The total surface drift current and the surface Stokes transport are shown in figure 6(*a*). The Stokes transport is seen here to vary between 5 and 13 % of the total surface drift. It is noted that, as soon as the waves become very steep and start to break at high wind velocities, the transport estimated from (2) and (3), which is applicable in principle only for small amplitude surface waves, may be in error.

Wind-induced surface drift

The difference between the total surface drift current and the Stokes surface transport is interpreted here as the wind-induced surface drift. The wind friction velocity is the sole parameter for correlating this component. The ratio between the wind-induced surface drift V_n and the wind friction velocity is plotted in figure 6(*b*); this ratio is seen to vary between 0·4 and 0·7. The variation of the surface drift with the wind velocity is not fully understood and needs more study; roughly, the following empirical expression is obtained:

$$V_n/u_{*a} = 0{\cdot}53. \tag{4}$$

Earlier results for surface drift currents (Keulegan 1951; Baines & Knapp 1965; Wu 1968; Plate 1970) were compiled by Wu (1973*a*). Despite the different water depths and wind conditions in their tanks and the various techniques for measuring surface drift adopted, the data (V_n/u_{*a}) as a whole have no obvious systematic dependence upon the wind friction velocity. The

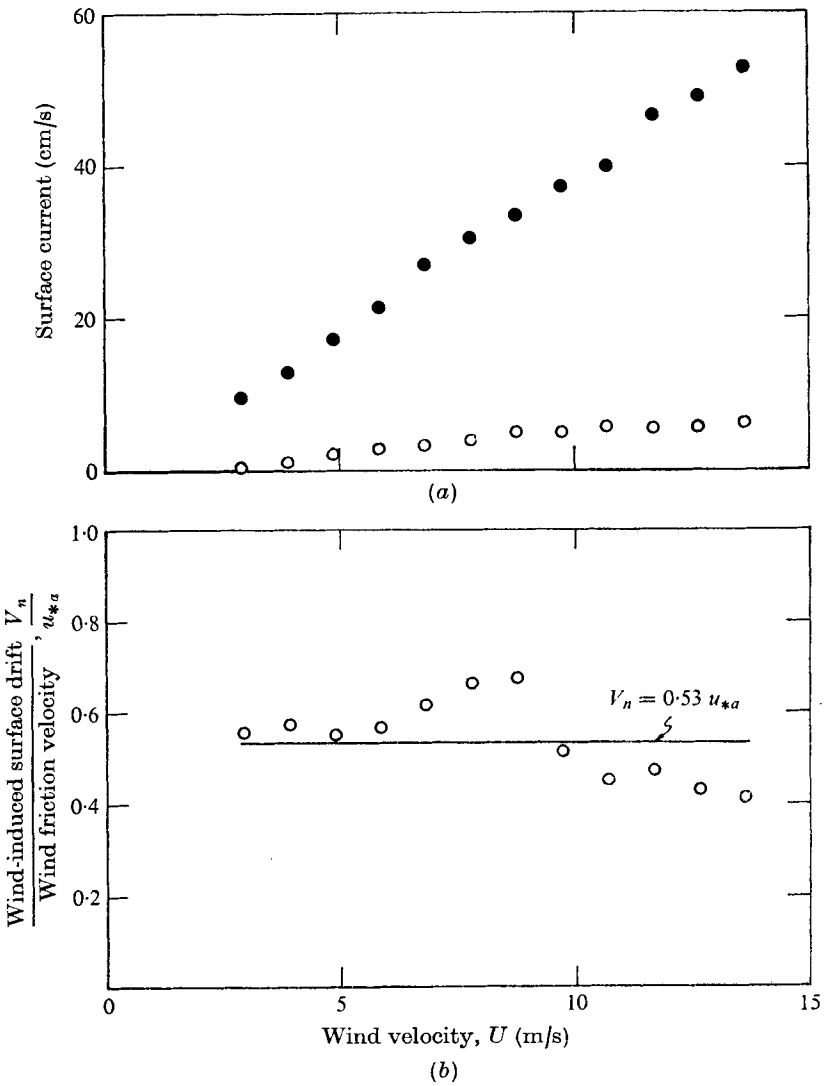

FIGURE 6. Wind-induced and wave-induced surface currents for various wind velocities. ●, total surface drift current; ○, wave-induced surface current in (*a*).

compiled data on the surface drift current, including the Stokes transport, were averaged and were shown to be reasonably well approximated by

$$V/u_{*a} = 0{\cdot}55. \tag{5}$$

There is no discrepancy between the present and the earlier results, as the Stokes surface transport in laboratory tanks is in most cases about 10 % or less of the total surface drift current. It is noted that the wind-induced drift was also measured recently by Phillips & Banner (1974) in the wind–wave tank, and their results indicated a value of $0{\cdot}55u_{*a}$ for the surface drift.

5. Near-surface drift currents

5.1. *Stokes current*

The surface mass transport predicted by Stokes (1847) is given in (3), and compares favourably with the experimental results. As discussed earlier, the Stokes current at the surface in the present tank varies between 5 and 13 % of the total surface drift. The subsurface Stokes current can be calculated by substituting into (2) the average values of the wave frequency and the wave height shown in figure 3. Relative to the measured subsurface drift current, to be shown later, the contribution of the Stokes current to the total drift current decreases with increasing depth: down to about half of the surface contribution at a depth of 2 cm, and down to about a quarter of the surface contribution at a depth of 4 cm.

For the subsurface current, Longuet-Higgins (1953) suggested that the mass transport in a wave tank is strongly influenced by viscous boundary layers at the bottom and at the free surface. Because of the small contributions of the Stokes current and uncertainty as to the effects of both the surface and bottom boundary layers on the mass-transport velocity, no attempt is made to separate the subsurface wind-induced current and wave-induced current. The total drift current measured in the present tank, discussed in the next subsection, is considered as the wind drift.

Currents measured with submerged floats

If the Kármán–Prandtl velocity distribution for hydrodynamically smooth flow (Schlichting 1968, p. 567) is applicable to the wind drift, it can be written as

$$\frac{v_c}{u_*} = \frac{V-v}{u_*} = 2{\cdot}5 \ln\left(\frac{zu_*}{\nu}\right) + 5{\cdot}5, \tag{6}$$

where v_c is the current relative to the water surface, u_* is the friction velocity of the wind-induced drift and ν is the kinematic viscosity of water. If the subsurface boundary layer is hydrodynamically rough with a roughness length z_0, (6) can be rewritten as

$$(V-v)/u_* = 2{\cdot}5 \ln (z/z_0) + 8{\cdot}5. \tag{7}$$

For each wind velocity, the currents at various depths near the surface were measured with floats of different submergences. The measurements at each depth were repeated at least six times. From the average of the measured currents and the surface drift indicated by the curve shown in figure 5(*b*), the current relative to the moving water surface was obtained and is plotted versus the depth in figure 7. The origin of the vertical axis for each profile is shifted so that all the current data can be plotted in the same figure.

It may be seen from figure 7 that the current in the upper layer varies linearly with the logarithm of the depth below the surface. A solid line is fitted to each profile on the basis of the least-squares principle. As shown in figure 5, the currents measured with surface floats very close to the water surface tend to follow a linear profile, and are not included here. These two sets of measurements will be compared further in a later section.

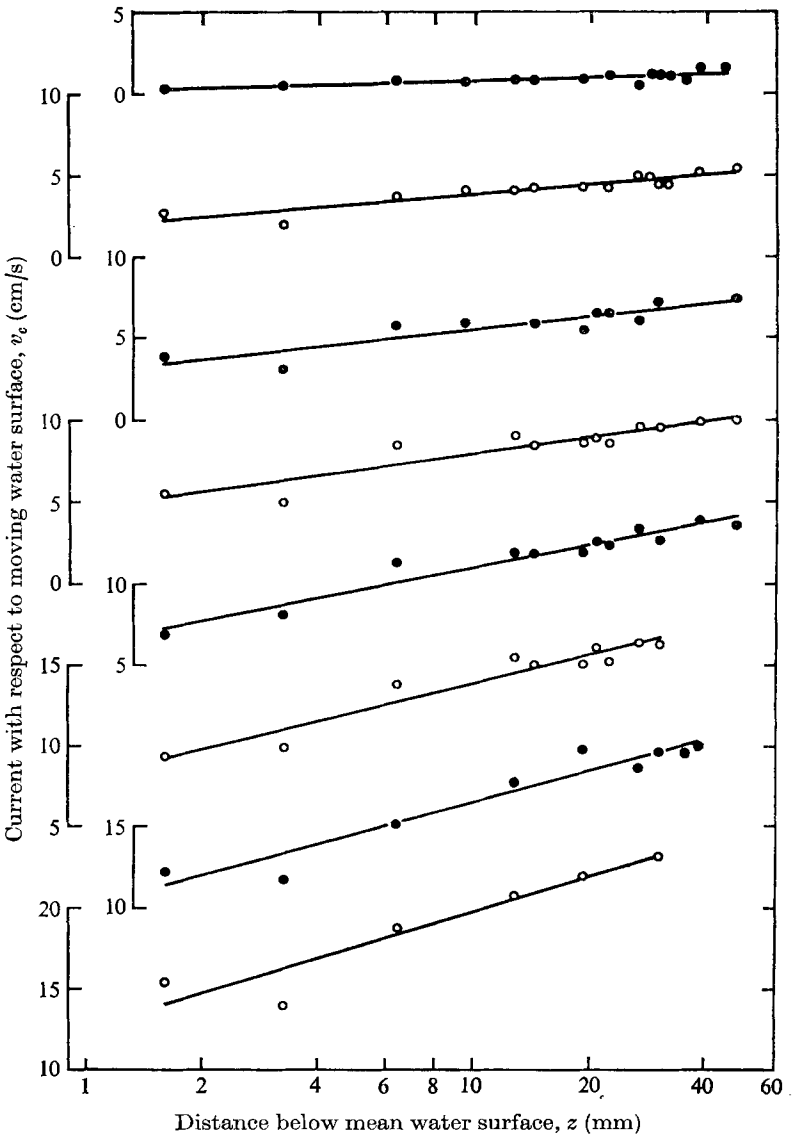

FIGURE 7. Current distributions near water surface measured with submerged floats. The wind velocities from top to bottom are U = 0·95, 1·91, 2·86, 3·81, 4·76, 5·72, 6·67 and 7·62 m/s.

Currents measured with fixed probe

For each wind velocity, the Pitot–static tube was placed at various depths to measure the wind drift near the water surface. The tube was placed at each depth for a period of 2 min. The dynamic pressure, sensed by a differential pressure transducer and recorded on tape, was later averaged on an analog computer to determine the local current. The averaged local current with respect to the moving water surface is plotted in figure 8 versus the depth below the mean water surface. A straight line is seen here again to fit closely the data, indicating that

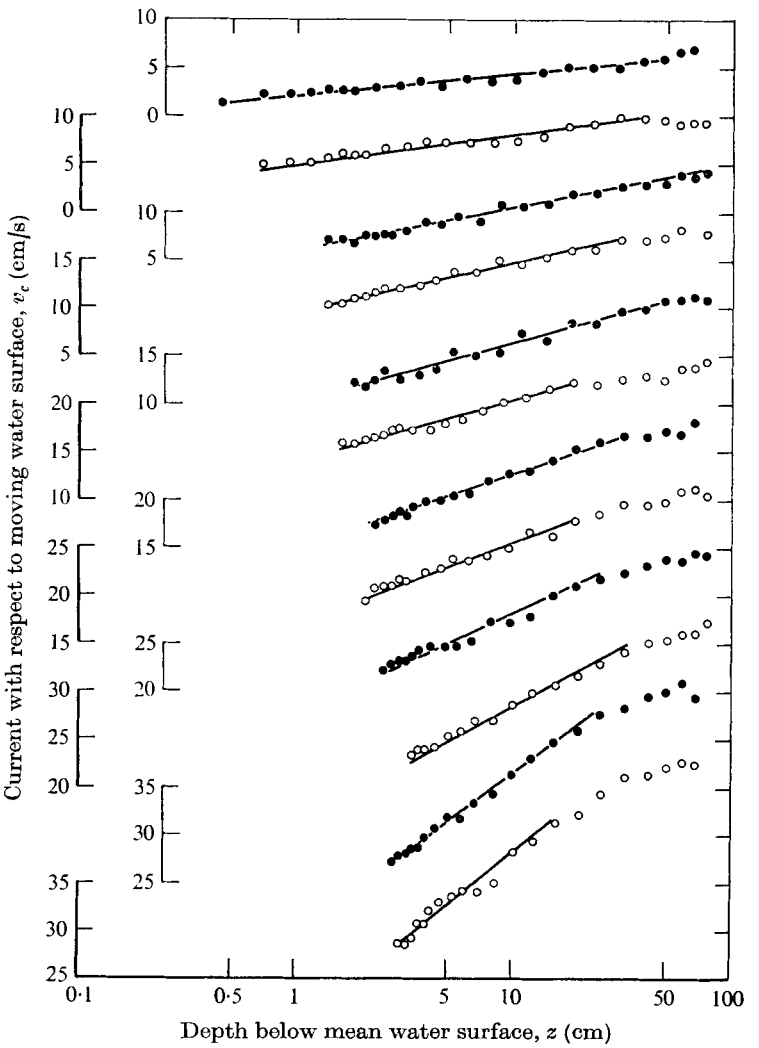

FIGURE 8. Drift currents measured with a fixed probe. The profiles from top to bottom are obtained at wind velocities U = 2·84, 3·82, 4·75, 5·71, 6·66, 7·64, 8·58, 9·51, 10·48, 11·45, 12·34 and 13·34 m/s.

the current measured with a fixed probe varies with the logarithm of the mean depth.

The currents measured at depths less than twice the wave amplitude below the mean water surface are not shown in figure 8. This omitted portion of data is generally very scattered and appears to deviate from the logarithmic profile. The scatter is undoubtedly due to measurement difficulties near the moving and undulating water surface, and the deviation is believed to be related to the motion induced by waves (Benjamin 1959; Phillips 1966, p. 89).

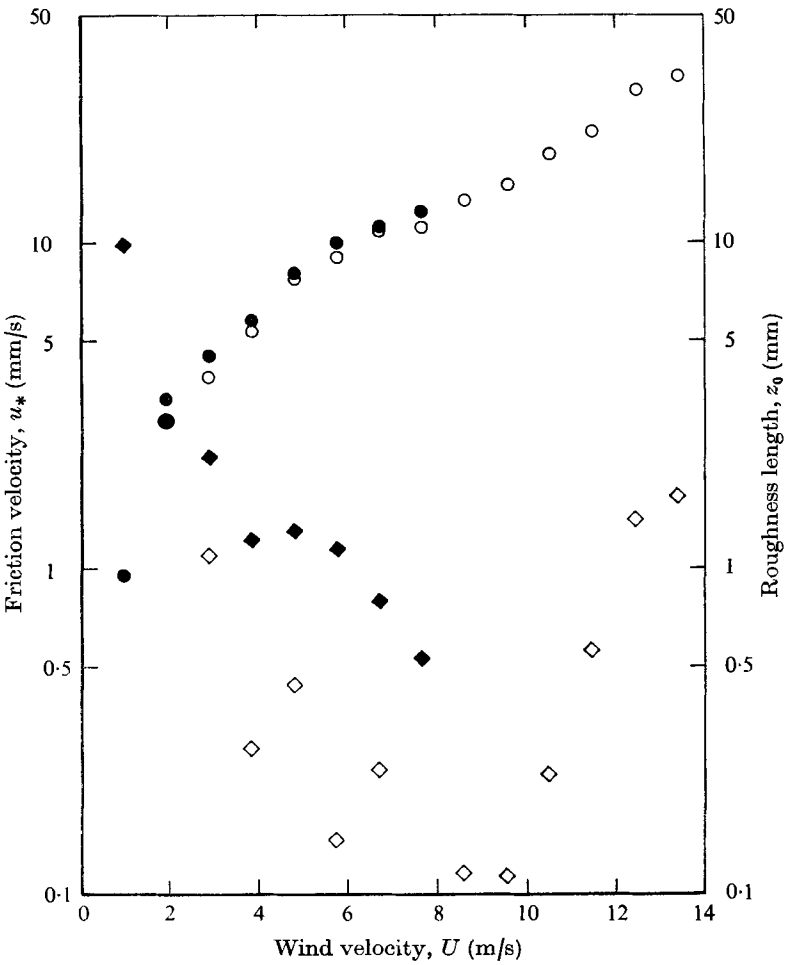

FIGURE 9. Friction velocity of current and roughness length of current boundary layer. Solid symbols, data obtained with submerged floats; open symbols, data obtained with a fixed probe. ○, u_*; ◇, z_0.

Friction velocity and surface roughness

The friction velocity of the current and the roughness length of the current boundary layer, obtained from the logarithmic current profile, are plotted in figure 9. The friction velocity and the roughness length of the current are seen to vary with the wind velocity in the same fashion as those of the wind, shown in figure 2. The friction velocities for the current are much smaller than those for the wind owing to the large density difference between water and air. The density difference, however, has no influence on the roughness length. The friction velocities of the current and of the wind will be further compared in a later section.

Comparing again the data shown in figures 2 and 9, the roughness lengths for the current are smaller than but comparable with those for the wind at low wind velocities and are much smaller than those for the wind at high wind velocities.

This trend is interesting. The difference is small at low wind velocities in the regime of wind–wave interaction governed by surface tension (Wu 1968), where capillary waves provide the roughness elements for the wind. At high wind velocities in the gravity-governed regime of wind–wave interaction (Wu 1968), the waves become cusp shaped at the crests and airflow separation also occurs there; the wave troughs, however, remain flat. Crests are the tops of the roughness elements for the wind and troughs are the tops of the roughness elements for the current.

The friction velocities determined with the submerged floats are seen in figure 9 to be in very close agreement with those determined with a fixed probe. These are indeed very interesting results. From the measurements with the floats which stayed at *constant* designated depths below the *undulating* water surface, we confirm, as conjectured by others (Phillips 1966), that the flow in the boundary layer over a wavy surface in which separation does not occur is bent to follow the surface configuration. The airflow in the present tank has been considered (Wu 1968, 1970) to separate from the dominant waves at high wind velocities, where the wind boundary layer is hydrodynamically rough. As discussed in a later section, the current boundary layer in the present tank, however, is always hydrodynamically smooth, so no flow separation is expected. There has been some concern over the distortion of the logarithmic velocity profile by the wave-induced motion (Phillips 1966, p. 141). The present results appear to indicate that the wave-induced disturbances vanish at a mean depth twice the wave amplitude.

There are some discrepancies between the roughness lengths measured with surface floats and with a traversing probe; see figure 9. More study is required to resolve this discrepancy; however, it may be worthwhile to mention that the roughness length is probably ill defined here, as the current boundary layer is hydrodynamically smooth.

6. Discussion

Regimes of wind and current boundary layers

The local Reynolds numbers R_x for both the atmospheric and aqueous boundary layers at the test section are given, respectively, by UL/ν_a and VL/ν, where L is the distance between the tunnel entrance and the test section. The results, shown in figure 10(*a*), indicate that for the same wind velocity the Reynolds number for the wind is always greater than that for the current. The transition of the boundary layer over a solid surface from laminar to turbulent generally occurs at $R_x \doteqdot 5 \times 10^5$ (Schlichting 1968, p. 435). If this result is applicable here, the current boundary layer at low wind velocities appears to be viscous, and the transition from viscous to turbulent flow occurs at $U = 3$ m/s.

The roughess Reynolds numbers R_k for both the wind and the current boundary layers are plotted in figure 10(*b*). The division of the boundary-layer regime (Schlichting 1968, p. 585) is also shown in the same figure. The wind boundary layer, as discussed elsewhere (Wu 1968, 1970), has two regimes, both of which are actually, or very nearly, hydrodynamically rough. Capillary waves serve as

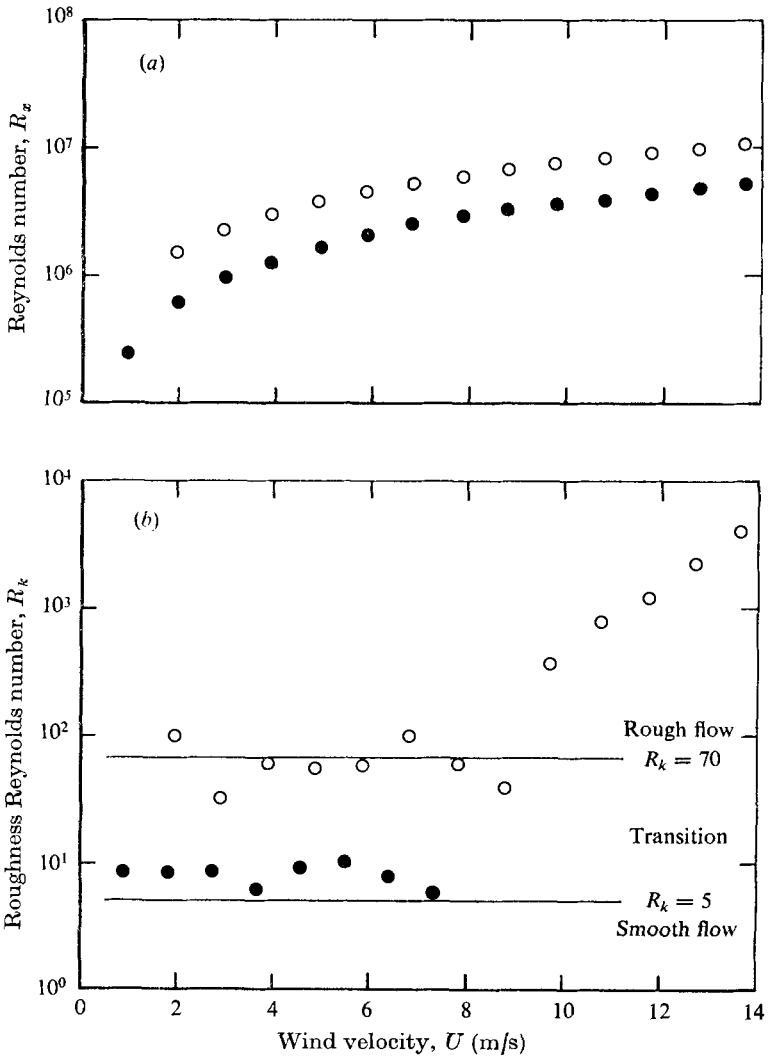

FIGURE 10. Regimes of wind and current boundary layers. ○, the atmospheric boundary layer; ●, aqueous boundary layer. The data used here for the aqueous boundary layer are those obtained with floats.

roughness elements at low wind velocities, where R_k increases gradually with U; gravity waves serve as roughness elements at high wind velocities, where R_k increases rapidly with U. The current boundary layer appears to be hydrodynamically smooth at low wind velocities. The data used here to calculate the roughness Reynolds number were those obtained with submerged floats. The roughness Reynolds number calculated with the data obtained with the traversing probe should be even smaller; see figure 9.

In summary, comparing the results for both boundary layers shown in figure 10, we see that the transitions of the current boundary layer to various regimes lag behind, or occur at wind velocities higher than, those of the wind boundary layer.

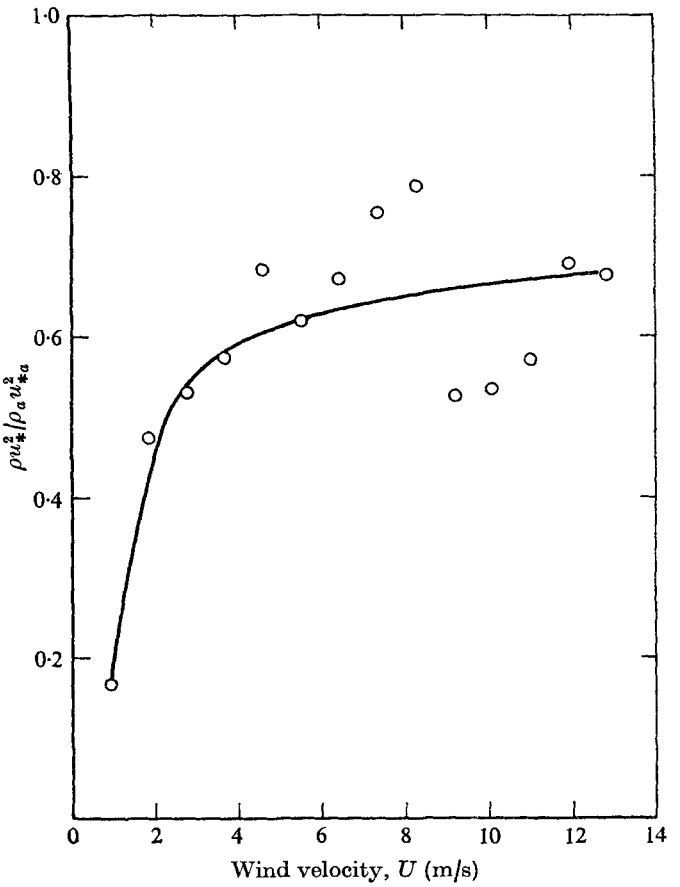

FIGURE 11. Momentum flux from wind to drift currents.

Wind stress and wave drag

The stress exerted by a flow on a solid rough boundary is completely supported by the form drag of roughness elements. In laboratory wind–wave tanks, the wind generates waves, which grow with the fetch. As the waves grow, their momentum also increases and extracts a portion of the wind stress. This portion of the stress is the so-called wave drag (Stewart 1964), which is the rate of direct momentum transfer from the wind to the waves.

The ratio τ_c/τ_0 between the shear stresses exerted by the current and by the wind on the air–water interface, calculated from the respective friction velocities is plotted versus the wind velocity in figure 11. It may be seen that this ratio increases approximately from 0·2 to 0·7 as the wind velocity increases. If we consider the difference between τ_0 and τ_c as the wave drag, then this difference should be related to the wave growth. The present results are consistent with two earlier estimates (Wu 1968, 1973*b*) of wave drag from the spatial growth rate of the waves. The ratio between τ_c and τ_0 was found earlier to be about 0·2 in the present tank with wind velocities greater than 3·5 m/s, and the rising portion of this ratio

shown in figure 11 is very similar to that found more recently in a smaller tank where the wave characteristics are very similar to those in the present cases of low wind velocity.

It was shown earlier (Wu 1968, 1969*b*, 1970) that the wind stress can be correlated with the amplitude of waves from which the wind separates. These results indicate that these specific waves serve as the roughness elements for the wind, and imply that the wind stress is supported principally by pressure drag on these waves. A further interpretation of the results made by Lighthill (1971) substantiates the hypothesis that momentum transferred by wind stress goes principally to the waves themselves. The viscous dissipation of wave energy to convert the momentum eventually into shear currents was considered by Lighthill to be a very slow process. Such a process occurs only at low wind velocities in the present tank. At high wind velocities, wave breaking dissipates the excess energy introduced by the wind. Therefore, in this case, the momentum flux is converted much faster into current, explaining the fact that the wave drag, shown in figure 11, is smaller at high wind velocities than at low wind velocities.

Viscous sublayer of wind drift

The existence of a viscous sublayer below the air–water interface has been considered by various investigators (Wu 1972). The thicknesses of the viscous sublayer (δ_v) and the buffer layer (δ_b) near the interface were estimated, respectively, from the relations for the boundary layer over a solid surface (Schlichting 1968, p. 565),

$$\delta_v = 11{\cdot}6u_*/\nu, \quad \delta_b = 30u_*/\nu. \tag{8}$$

These thicknesses at low wind velocities were estimated from the friction velocities of the current, measured with submerged floats and shown in figure 9, and are plotted in figure 12. At very low wind velocities, the depth to which the currents were measured with surface floats, shown in figure 5, is seen to be comparable with the thickness of the viscous sublayer. For these cases, the friction velocity of the current can also be calculated from the velocity gradient $u_* = \nu\, dv/dy$, shown in figure 5.

The friction velocities determined from the linear profiles, shown in figure 5, are compared in figure 12 with those determined from the logarithmic profiles, shown in figure 7. The close agreement of the two sets of results at *very low* wind velocities indicates that a viscous sublayer indeed exists immediately below the air–water interface and heaves with the surface undulation. As the wind velocity increases, the viscous sublayer becomes thinner; the measurements with surface floats, shown in figure 5, extend beyond the viscous sublayer. Because the maximum velocity gradient occurs within the sublayer, the gradient determined from the straight line fitted to the data extending beyond the sublayer should be smaller than that within the sublayer. Consequently, the friction velocity determined from the linear profile deviates from, and becomes smaller than, the actual friction velocity, determined from the logarithmic profile.

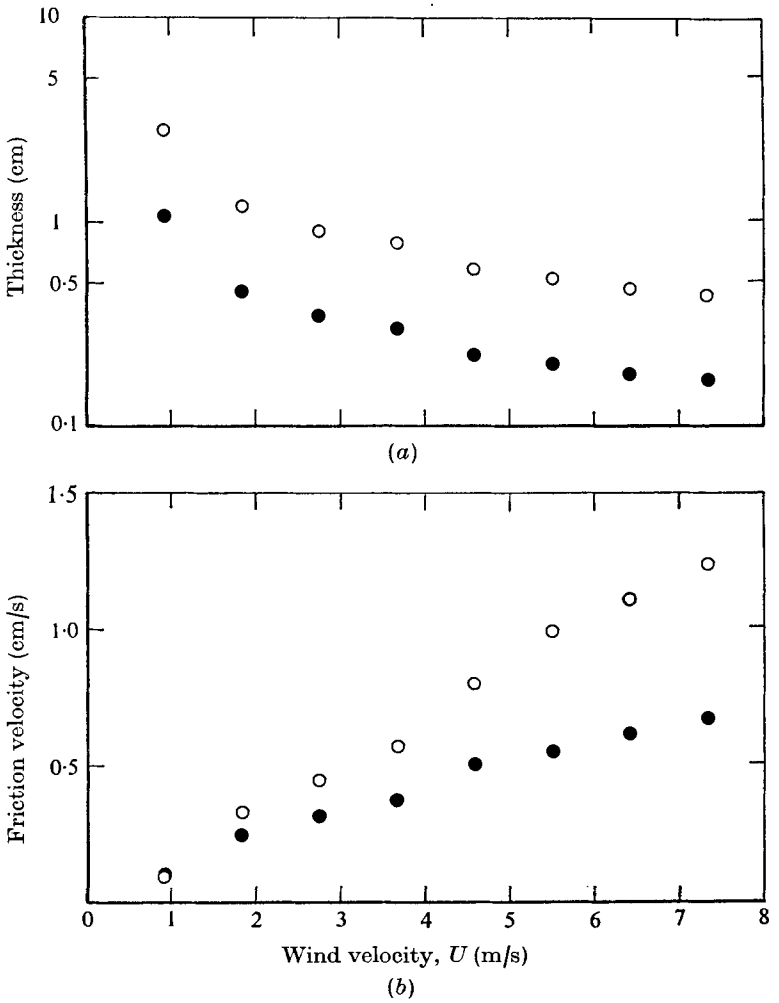

FIGURE 12. Comparison of friction velocities obtained from linear and logarithmic current profiles. (*a*) ○, buffer layer; ●, viscous sublayer. (*b*) ○, from logarithmic profile; ●, from linear profile.

Surface drift currents at various fetches

As discussed previously, the surface drift current has two components: the wind-induced shear current and the wave-induced Stokes current. The former is generated by the wind stress and the latter is related to wave characteristics. In order to determine the total surface drift current at various fetches, both components must first be separately estimated on the basis of the respective scaling laws, and then added to determine the total surface drift.

On the basis of the logarithmic wind velocity distribution above the disturbed water surface and an equation describing the equilibrium state of wind–wave interactions, a non-dimensional expression for determining wind-stress coefficients at all fetches has been suggested by Wu (1969*b*):

$$1/C_y^{\frac{1}{2}} = 2{\cdot}5 \ln (91/C_y F^2), \quad F = U_y/(gy)^{\frac{1}{2}}, \tag{9}$$

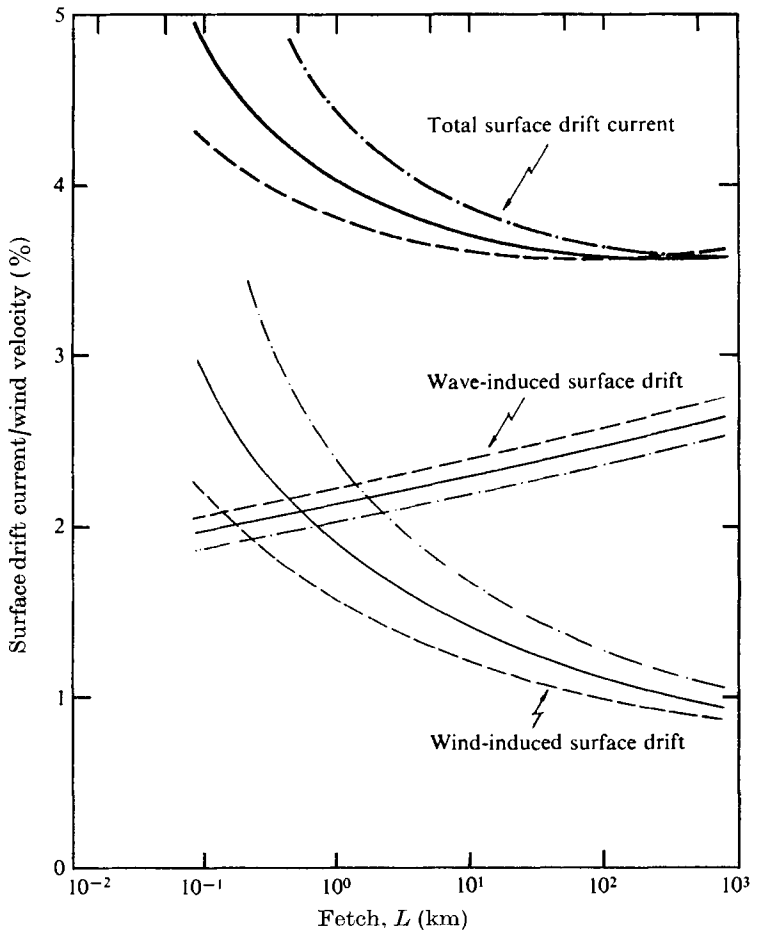

FIGURE 13. Variation of wind-induced and wave-induced surface drift currents with fetch. U_y (m/s): – – –, 5; ———, 10; — · —, 20.

where F is the Froude number, U_y is the wind velocity measured at an elevation y above the mean water surface, and C_y is the wind-stress coefficient, defined as $C_y = \tau_0/\rho_a U_y^2$. Since the scaling law is derived from the logarithmic wind profile, the anemometer should be close enough to the water surface to be within the logarithmic-profile region, and should be also far enough from the water surface to avoid wave-induced air motion. Such an anemometer height was proposed (Wu 1971) to be

$$y = \begin{cases} 7{\cdot}35 \times R_*^{\frac{3}{2}} \times 10^{-7}\,\text{m}, & R < 5 \times 10^{10}, \\ 10\,\text{m}, & R > 5 \times 10^{10}, \end{cases} \tag{10}$$

where $R = U_y L/\nu_a$ is the fetch Reynolds number, U_y is the wind velocity measured at the proposed anemometer height and L is the wind fetch.

By combining (4), (9) and (10), the wind-induced surface drifts at various fetches can be determined, and are plotted in figure 13. Earlier results (Wu 1969*b*) have established that the wind-stres coefficient decreases with increasing fetch.

The present results indicate that the wind-induced surface drift is proportional to the wind friction velocity. Taken together, the ratio between the wind-induced surface drift and the wind velocity decreases with increasing fetch.

Wave data obtained at various fetches were compiled by Wiegel (1964, p. 216) and faired by Wu (1969*c*) with the following results:

$$c/U_y = 0{\cdot}0502(gL/U_y^2)^{0{\cdot}3}$$

and

$$gH_{\frac{1}{3}}/U_y^2 = 0{\cdot}0031(gL/U_y^2)^{0{\cdot}47}, \tag{11}$$

where c and $H_{\frac{1}{3}}$ are the phase velocity and the height of dominant waves, respectively. Substituting (11) into (3), we can find the Stokes surface transport at various fetches; see figure 13. Contrary to the trend for the wind-induced component, the wave-induced surface drift is seen to increase with the wind fetch.

The present calculation of wave drift differs from the calculations of Bye (1967), Chang (1969) and Kenyon (1970). They obtain the Stokes drift from a spectral average, while the sea is considered here as a narrow-band process. Undoubtedly, their procedure is more correct provided that no serious wave–wave interaction occurs. More study is definitely needed not only of the Stokes drift of random waves but also of the spectral description of short waves; there may be a significant contribution from short waves to the drift (Wright 1970). It suffices to say here that the present estimated wave drifts are in qualitative agreement with those obtained from the spectral average.

The sum of the wind-induced and the wave-induced components is the total drift. It may be seen in figure 13 that the total drift is approximately independent of the wind fetch and is about 3·5 % of the wind velocity at long fetches. This value is only slightly greater than the commonly accepted value of about 3 %. However, the last value is believed to be obtained with surface floats of appreciable sizes; as shown in figure 5, such floats generally indicate a smaller drift.

Shemdin (1972) suggested on the basis of his laboratory data that the surface drift was essentially a wind-induced shear current. On the other hand, Bye (1967) and Kenyon (1970) concluded from their analyses of oceanic wave data that the surface drift was primarily a wave-induced mass transport. The present results are helpful for resolving such a discrepancy; both arguments appear to indicate the trend but are overstated.

7. Conclusions

Systematic and simultaneous measurements have been made of the wind and current boundary layers as well as the wave characteristics in a wind–wave tank. The results show that the current varies logarithmically with the distance below the interface, and that the transitions of the current boundary layer to various regimes lag behind those of the wind boundary layer. Comparing the results obtained with submerged floats and with a traversing probe, we see that the current flow is bent to follow the surface configuration. The results obtained with surface floats immediately below the water surface do not conflict with the general consideration that a viscous sublayer exists just below the interface. Direct measurements are presented of the portion of the wind stress effective

in generating currents. This has been discussed indirectly elsewhere, and is shown here to be related to the wave characteristics. Two components of the surface drift, the wind-induced shear current and wave-induced mass transport, are separately scaled and estimated. Expressed as fractions of the wind velocity, the former component was found to decrease and the latter component to increase with increasing fetch; the total surface drift was found to decrease gradually with increasing fetch and to approach a constant value.

This work was supported by the Office of Naval Research under Contract N00014-73-C-0091. I am very grateful to Mr N. Lewis for conducting the experiment.

REFERENCES

BAINES, W. D. & KNAPP, D. J. 1965 Wind driven water currents. *J. Hyd. Div. A.S.C.E.* **91**, 205–221.

BENJAMIN, T. B. 1959 Shearing flow over a wavy boundary. *J. Fluid Mech.* **6**, 161–205.

BYE, J. A. T. 1965 Wind-driven circulation in unstratified lakes. *Limnol. Oceanogr.* **10**, 451–458.

BYE, J. A. T. 1967 The wave-drift current. *J. Mar. Res.* **25**, 95–102.

CHANG, M. S. 1969 Mass transport in deep-water, long-crested random gravity waves. *J. Geophys. Res.* **74**, 1515–1536.

COX, C. S. 1958 Measurements of slopes of high-frequency wind waves. *J. Mar. Res.* **16**, 199–225.

KENYON, K. E. 1970 Stokes drift for random gravity waves. *J. Geophys. Res.* **74**, 6991–6994.

KEULEGAN, G. H. 1951 Wind tides in small closed channels. *J. Res. Nat. Bur. Stand.* **46**, 358–381.

LIGHTHILL, M. J. 1971 Time-varying currents. *Phil. Trans.* A **270**, 371–390.

LONGUET-HIGGINS, M. S. 1953 Mass transport in water waves. *Phil. Trans.* A **245**, 535–581.

PHILLIPS, O. M. 1966 *The Dynamics of the Upper Ocean.* Cambridge University Press.

PHILLIPS, O. M. & BANNER, M. L. 1974 Wave breaking in the presence of wind drift and swell. *J. Fluid Mech.* **66**, 625–640.

PLATE, E. J. 1970 Water surface velocity induced by wind shear. *J. Engng Mech. Div. A.S.C.E.* **96**, 295–312.

RUSSELL, R. C. H. & OSORIO, J. D. C. 1957 An experimental investigation of drift profiles in a closed channel. *Proc. 6th Conf. Coastal Engng, University of California, Berkeley*, pp. 171–193.

SCHLICHTING, H. 1968 *Boundary Layer Theory.* McGraw-Hill.

SHEMDIN, O. H. 1972 Wind-generated current and phase speed of wind waves. *J. Phys. Oceanogr.* **2**, 411–419.

STEWART, R. W. 1964 The wave drag of wind over water. *J. Fluid Mech.* **10**, 189–194.

STOKES, G. G. 1847 On the theory of oscillating waves. *Proc. Camb. Phil. Soc.* **8**, 441–445.

WIEGEL, R. L. 1964 *Oceanographical Engineering.* Prentice-Hall.

WRIGHT, J. W. 1970 Stokes drift and the fully developed sea. *J. Geophys. Res.* **75**, 2847–2848.

WRIGHT, J. W. & KELLER, W. C. 1971 Doppler spectra in microwave scattering from wind waves. *Phys. Fluids*, **14**, 466–474.

WU, J. 1968 Laboratory studies of wind–wave interactions. *J. Fluid Mech.* **34**, 91–112.

WU, J. 1969*a* An estimation of wind effects on dispersion in wide channels. *Water Resources Res.* **5**, 1097–1104.

Wu, J. 1969*b* Froude number scaling of wind-stress coefficients. *J. Atmos. Sci.* **26**, 408–413.

Wu, J. 1969*c* Wind stress and surface roughness at air–sea interface. *J. Geophys. Res.* **74**, 444–455.

Wu, J. 1970 Wind–wave interactions. *Phys. Fluids*, **13**, 1926–1930.

Wu, J. 1971 Anemometer height in Froude scaling of wind stress. *J. Waterways Harbors Coastal Engng Div. A.S.C.E.* **97**, 131–137.

Wu, J. 1972 An estimation of oceanic thermal sublayer thickness. *J. Phys. Oceanogr.* **1**, 284–286.

Wu, J. 1973*a* Prediction of near-surface drift currents from wind velocity. *J. Hyd. Div. A.S.C.E.* **99**, 1291–1302.

Wu, J. 1973*b* Wind-induced turbulent entrainment across a stable density interface. *J. Fluid Mech.* **61**, 275–87.